2008 IEEE International Conference on
Robotics and Automation
Pasadena, CA, USA, May 19-23, 2008

Kinematics and Calibration of Active Cannulas

Robert J. Webster III
Mechanical Engineering
Vanderbilt University
Nashville, TN 37235

Joseph M. Romano
Mechanical Engineering
Univeristy of Pennsylvania
Philadelphia, PA 19104

Noah J. Cowan
Mechanical Engineering
The Johns Hopkins University
Baltimore, Maryland 21218

***Abstract*— Active cannulas are remotely actuated thin continuum robots with the potential to traverse narrow and winding environments without relying on "guiding" environmental reaction forces. These features seem ideal for procedures requiring passage through narrow openings to access air-filled cavities (e.g. surgery in the throat and lung). Composed of telescoping concentric pre-curved elastic tubes, an active cannula is actuated at its base by translation and axial rotation of component tubes. Using minimum energy principles and Lie Group theory, we present a framework for the kinematics of multi-link active cannulas. This framework permits testing of the hypothesis that overall cannula shape locally minimizes stored elastic energy. We evaluate in particular whether the torsional energy in the long, straight transmission between actuators and the curved sections is important. Including torsion in the kinematic model enables us to analytically predict experimentally observed bifurcation in the energy landscape. Independent calibration procedures based on bifurcation and tip and feature positions enable model parameter identification, producing results near ranges expected from tube material properties and geometry. Experimental results validate the kinematic framework and demonstrate the importance of modeling torsional effects in order to describe bifurcation and accurately predict active cannula shape.**

I. Introduction

Robotic dexterity at the "meso scale"—from hundreds of microns to tens of centimeters—involves challenges in fabrication, modeling, and control. Continuously flexible ("continuum") robots are a promising class of robots for this scale, provided they can be sufficiently miniaturized. Current designs require wires [3], [6], flexible push rods [13], pneumatic actuators [2], [7], or other external actuation mechanisms that can limit miniaturization.

Here, we describe active cannulas, a new class of miniature continuum robots, that exhibit robotic dexterity at this scale and seem well suited for working in confined or tortuous environments. Our principle motivation for creating the active cannula design is interventional medicine, where we expect them to provide minimally invasive access to many challenging or currently unreachable surgical sites.

The active cannula design simultaneously has a small diameter and high degree of dexterity by incorporating pre-curved telescoping tubes in its backbone rather than external tendon wires or other force transmission mechanisms (Figure 1). Elastic interaction of the curved tubes as they are axially rotated and translated with respect to one another makes an active cannula sufficiently flexible and shapable to traverse challenging anatomy. Importantly, active cannula dexterity improves with miniaturization and inherent compliance may enhance safety [17].

A number of clinical applications may substantially benefit from active cannulas, and similar designs have been proposed for fetal surgery [5], steering needles in soft tissues [8] and cardiac applications [11], transnasal skull base surgery [17], and transgastric surgery [17]. Several specific clinical areas in which active cannulas could improve surgical outcomes are described in detail in [14]. In many of these applications initial free-space cannula models (to date, only free-space models exist) will need to be coupled with tissue models. However, free-space models alone should be sufficient for applications characterized by air-filled passageways, such as surgery in the throat and lung.

Each active cannula application will require customization of the design, and we foresee a family of both hand-held and robotically actuated active cannulas tailored to meet various clinical needs. However, nearly all foreseeable applications will require an accurate forward kinematic description of active cannula shape as a function of joint angles (translations and rotations of component tubes), which is the focus of this paper. Such a model serves not only as a starting point for more complex cannula/tissue interaction modeling, but is also directly applicable in free-space medical scenarios like the throat and airways.

II. Related Work

Active cannulas change shape using pre-curvature and differential motion of superelastic component tubes. While the location of actuation is similar to other medical devices like catheters and steerable needles (at the base, outside the body), we emphasize that active cannulas utilize a fundamentally

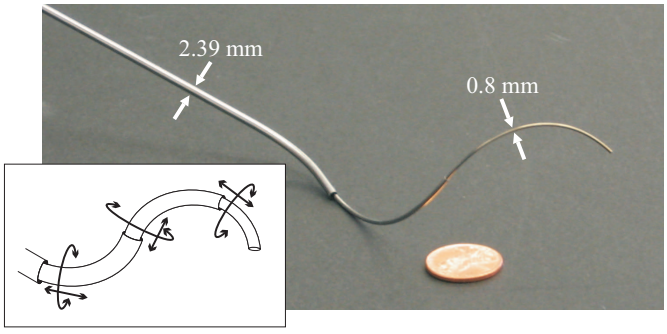

Fig. 1. A prototype active cannula made of superelastic nitinol tubes. The inset line drawing indicates the active cannula's degrees of freedom. (Adapted from [17]).

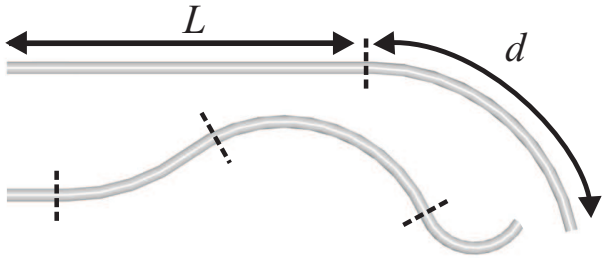

Fig. 2. (Top) Tubes used in all active cannula studies to date (including this paper), consist of a straight transmission of length L, with a constant curvature section of length d at one end. (Bottom) However, our models are in principle general enough to account for piecewise circular/straight tubes with multiple transition points.

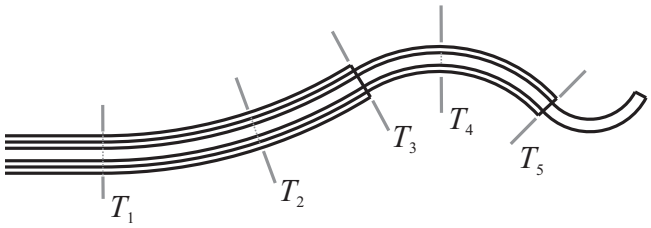

Fig. 3. The "links" or regions of unique overlap of a 3-tube cannula composed of tubes like those in Figure 2–Top. Links start and end at transition points, and the j^{th} link is between T_j and T_{j+1}. The largest tube transitions from straight to the left of T_1 to curved to the right. The same is true of the middle tube at T_2 and the smallest tube at T_4.

different means of steering within the body. Catheters use blood vessel reaction forces to direct them down desired branches. Steerable needles generate bending via tissue reaction forces that arise as they manuver through a soft tissue medium [10], [15], [16]. In contrast to catheters and steerable needles, active cannulas do not require vessel or tissue reaction force to steer. This does not preclude their use as steerable needles (when coupled with tissue models), and multi-lumen steerable needles based on pre-curvature have been proposed [4], [8]. However, it does mean that active cannulas are perhaps better classified as continuum robots. They can be considered miniature serial robot arms composed of variable curvature prismatic links.

Within the context of continuum robots, active cannulas are unique in their use of the backbone itself to transmit bending forces. Continuum robots typically use an initially straight elastic backbone, which is bent by forces applied through external mechanisms like wires (e.g. [3], [6]), flexible push rods [13], or pneumatic actuators (e.g. [2], [7]). While these external mechanisms are advantageous in permitting direct control of curvature, they also limit miniaturization. This motivates our desire to build bending actuation directly into the backbone itself.

Initial studies of active cannulas have either not modeled curved tube interaction [5], or provided beam-mechanics-based models [11], [17]. Developed concurrently and independently, these models are strikingly similar. Though parametrized slightly differently, both describe arc parameters of concentric segments of curved elastic tubes as a function of base angles of rotation. Both do so through computing the equilibrium of applied moments, under similar assumptions. One difference between the two studies is torsion, which is assumed negligible in [11], and included in transmission (the straight segments beginning at the actuators and ending at the start pre-curved tube regions) in [17]. Without torsion, the kinematics of an active cannula can be expressed in closed form. Including torsion in transmission leads to transcendental equations that must be numerically solved. While a framework for multi-link forward and inverse kinematics without torsion has been formulated [12], it has not yet been experimentally validated. Thus, our objectives in the following sections are to a derive multi-link kinematic framework that includes torsion, to determine model parameters via calibration, and to experimentally assess the the accuracy and descriptive capability of models with and without torsion.

III. The Active Cannula

The active cannula shown in Figure 1 is made of three pre-curved nitinol tubes, with a largest section diameter of 2.4 mm, tapering to a smallest section diameter of 0.8 mm. We note that this prototype has not been optimized for any particular application. Smaller tubes can be used, inter-tube tolerances can be reduced, and precurvatures can be chosen to suit a particular application. While it is often challenging to add additional bending sections to other continuum robot designs, an important feature of the active cannula is that additional sections can be easily added by increasing the number of tubes.

Forward kinematics for an active cannula is a description of the complete device shape in terms of joint variables, namely component tube linear positions and axial rotations. This requires a model of how pre-curved tubes cause one another to bend. A one "link" model was developed in [17], which maps from the axial rotation angles of n concentric curved tubes to their common equilibrium curvature and bending plane. The main (experimentally validated) assumptions in this model are that tubes can be considered to directly apply moments to one another, and that (due to circular component tube pre-curvatures) those moments can be considered constant along the length of the link.

All previous studies mentioned above [4], [5], [8], [11], [12], [17] have restricted themselves to component tubes that have a straight transmission with a circular constant curvature section at one end. While such component tubes are also our primary concern in this paper, we note that the models presented here are general enough to account for component tubes that have (or can be approximated as having) multiple constant curvature and straight sections along their lengths, as illustrated in Figure 2.

IV. Forward Kinematics

The forward kinematics of continuum and hyperredundant robots is often decomposed into two mappings. One is from

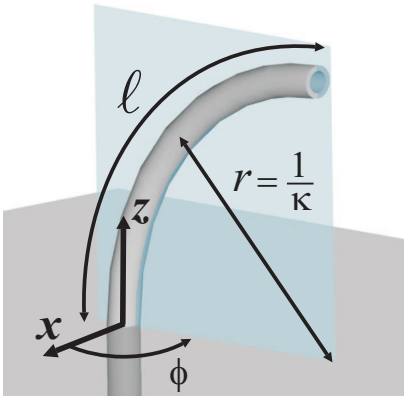

Fig. 4. The arc parameters of a link of curved tube consist of curvature (κ), equilibrium plane angle (ϕ), and arc length (ℓ_j), respectively).

actuator (joint) space to arc parameters (curvature, plane, and length of each section), while the other is from arc parameters to Cartesian positions of the robot. We follow a similar strategy in the analysis of the active cannula. The first mapping (Sections IV-A and IV-B) is generally robot-specific, since the type of actuators and design of the robot strongly influence how actuators affect arc parameters. The mapping from arc parameters to shape (Section IV-C), on the other hand, is common to all robots that can be modeled as piecewise constant curvature.

The shape of an active cannula is defined by a sequence of unique overlap regions ("links") between transition points T_j, as shown in Figure 3. Each of these links remains circular (although the bending plane and curvature change) as tubes are axially rotated [11], [17]. Thus, an active cannula has piecewise constant curvature, consisting of a series of constant curvature links tangent to adjacent links.

A. Determining Link Lengths

The first step in describing the shape of an active cannula is determining the number of links and link lengths. These are defined by component tube transition point locations, which are functions of tube pre-shaped geometry (Figure 2) and translational joint positions of tube bases. These combine to create a sequence of links between transition points as shown in Figure 3. For the 3-tube active cannula illustrated (where each tube has a straight transmission followed by a single circular arc), there are 5 curved links. More generally, n tubes result in $2n-1$ links. The length of some links reach zero when transition points align. It is straightforward to determine the lengths of the links in the cannula, given actuator displacements and component tube geometries.

For the example in Figure 3 the lengths of the m (in this case five) regions of overlap $\ell_j, j \in \{1,\dots,m\}$ are given by the actuator translational positions of the n tubes $\rho_i, i \in \{1,\dots,n\}$, and the lengths of the curved portion d_i of each tube as,

$$\begin{aligned} \ell_1 &= \rho_2 - \rho_1, & \ell_4 &= \rho_2 + d_2 - \rho_3, \\ \ell_2 &= \rho_1 + d_1 - \rho_2, & \ell_5 &= \rho_3 + d_3 - \rho_2 - d_2. \\ \ell_3 &= \rho_3 - \rho_1 - d_1, \end{aligned} \tag{1}$$

A general procedure easily amenable to software implementation for determining all ℓ_j is to sort transition points in terms of arc length, with link lengths given by differences between adjacent transition points. We also note that if component tubes themselves have more than one transition point, additional active cannula links are the result.

B. From Joint Space to Arc Parameters

Active cannula joint space is parametrized by axial translations, ρ, and rotations, α, applied at the base of each tube, namely $q = (\rho_1, \alpha_1, \dots, \rho_n, \alpha_n)$. In what follows, the subscript $i \in \{1,\dots,n\}$ refers to tube number, while $j \in \{1,\dots,m\}$ refers to link number. Cannula links are circular segments described by the arc parameters curvature, plane, and arclength (κ, ϕ, and ℓ), as shown in Figure 4. The mapping from q to ℓ was described in the previous section, while the mapping from q to (κ, ϕ) can be accomplished by generalizing the model in [17] as follows.

Attach a coordinate frame, T_j, at the base of the link by sliding a copy of the cannula base frame along the backbone (without rotation about z) to the base of the link. The model then yields x and y curvature components for the link in the link frame as

$$\chi_j = \frac{\sum_i E_i I_i k_{i,j} \cos\theta_{i,j}}{\sum_i E_i I_i} \text{ and } \gamma_j = \frac{\sum_i E_i I_i k_{i,j} \sin\theta_{i,j}}{\sum_i E_i I_i}$$

respectively. The sums over $i \in \Lambda_j$ only include the tubes that overlap the j^{th} link. Since the intrinsic (preformed) curvature is piecewise constant along each tube, $k_{i,j}$ denotes the intrinisic curvature of the i^{th} tube in the j^{th} link. Note that these values change as a function of the actuator translations, because the overlapping regions change as described above, i.e. $k_{i,j} = k_{i,j}(\rho)$. E_i is the elastic modulus, I_i is the cross sectional moment of inertia, and $\theta_{i,j}$ is the axial i^{th} tube angle about the j^{th} link frame z axis. There is a direct relationship between curvature components and arc parameters, namely

$$\phi_j = \tan^{-1}\left(\frac{\chi_j}{\gamma_j}\right), \quad \text{and} \quad \kappa_j = \sqrt{\chi_j^2 + \gamma_j^2}. \tag{2}$$

Neglecting torsional compliance completely (that is, assuming infinite torsional rigidity), $\theta_{i,j} = \theta_{i,0} \equiv \alpha_i$ for all j, which results in a direct symbolic mapping (2) from actuator space to arc parameters for each link. However, when transmissional torsion is included, $\theta_{i,1}$ no longer equals actuator input α_i, because the straight transmission will "wind up" as torque is applied at the actuators. Since transmissions are generally long compared to curved sections, we assume that tubes can be modeled as infinitely torsionally stiff beyond T_1, implying that $\theta_{i,j} = \theta_{i,1} \equiv \psi_i$, for all $j > 1$. With these definitions, the

total elastic energy stored in the system is given by

$$U(\psi_1,\ldots,\psi_n) = \underbrace{\sum_{i=1}^{n} \frac{G_i J_i}{2L_i}(\alpha_i - \psi_i)^2}_{\text{transmission torsion}} + \underbrace{\sum_{j=1}^{m}\sum_{i\in\Lambda_j} \frac{E_i I_i \ell_j}{2}(\chi_j - k_{i,j}\cos(\psi_i))^2}_{x \text{ direction bending}} + \underbrace{\sum_{j=1}^{m}\sum_{i\in\Lambda_j} \frac{E_i I_i \ell_j}{2}(\gamma_j - k_{i,j}\sin(\psi_i))^2}_{y \text{ direction bending}}, \quad (3)$$

where G is the shear modulus, J is the polar moment of inertia, and L is the length of straight transmission between actuator and curved section of tube.

We assume that actuator inputs influence the system "adiabatically" in the sense that as we move the actuators, the system remains at a local minimum of the energy landscape. Thus the angles at the end of the straight transmission $(\psi_1,\ldots,\psi_n)$ are always assumed to be at a local minimum of (3).

As we describe in Section V, there can be multiple stable local minima of (3). Thus the forward kinematics, given the actuator states, is not necessarily a unique mapping. The particular minimum of (3) in which the robot finds itself is dependent on the path traversed through through joint space to reach current joint angles.

To obtain the minimum of the energy function (3), one can solve for the critical points where the gradient equals zero. This leads to a set of transcendental equations, which can be solved numerically using a variety of techniques (e.g. Newton's method).

C. End-Effector Pose

The shape of the cannula is defined by the arc parameters and the product of exponentials formula. Using the notation of [9], the joint twists associated with arc parameters are,

$$\xi_\phi = \begin{bmatrix}0 & 0 & 0 & 0 & 0 & 1\end{bmatrix}^T,$$
$$\xi_j = \begin{bmatrix}0 & 0 & 1 & \kappa_j & 0 & 0\end{bmatrix}^T.$$

The full kinematics of the mechanism is then given by,

$$g = \prod_{j=1}^{m} e^{\left(\widehat{\xi_\phi}(\Delta\phi_j)\right)} e^{\left(\widehat{\xi_j}\ell_j\right)} \quad (4)$$

where $\Delta\phi_j = \phi_j - \phi_{j-1}$ and $g \in \mathrm{SE}(3)$ is the transformation from cannula base to tip. Thus, each cannula link contributes a pair of exponentials to the overall kinematics.

V. The $n = 2$ case

For the remainder of the paper we will consider the specific case of $n = 2$ which corresponds to the prototype with which we perform experimental validation and parameter fitting. For $n = 2$ we have $m = 2n - 1 = 3$ regions of overlap, only the middle of which contains two curved tubes. In this case the energy (3) is

$$U(\psi_1,\psi_2) = \frac{c_1}{2}(\alpha_1 - \psi_1)^2 + \frac{c_2}{2}(\alpha_2 - \psi_2)^2 + \ell_1 c_3 k_1^2 + \ell_2 c_3\left(\frac{k_1}{k_2} - 2\cos(\psi_1 - \psi_2) + \frac{k_2}{k_1}\right),$$

where $c_1 = \frac{G_1 J_1}{L_1}, c_2 = \frac{G_2 J_2}{L_2}$, and $c_3 = \frac{E_1 I_1 E_2 I_2}{E_1 I_1 + E_2 I_2}\kappa_1\kappa_2$. The gradient is then

$$\nabla U = \begin{bmatrix} -c_1(\alpha_1 - \psi_1) + \ell_2 c_3 \sin(\psi_1 - \psi_2) \\ -c_2(\alpha_2 - \psi_2) - \ell_2 c_3 \sin(\psi_1 - \psi_2)\end{bmatrix} = 0, \quad (5)$$

where the unknowns are (ψ_2, ψ_1), and (α_1, α_2) are the inputs.

Adding these two equations yields $\psi_2 = \frac{c_1}{c_2}(\alpha_1 - \psi_1) + \alpha_2$, which when substituted back into (5) yields

$$\psi_1 - \alpha_1 = \ell_2 b_1 \sin(\alpha_2 + b_2\alpha_1 - (1 + b_2)\psi_1), \quad (6)$$

where

$$b_1 = c_3/c_1 \quad \text{and} \quad b_2 = c_1/c_2. \quad (7)$$

The transcendental (6) can be approximately solved using a variety of techniques. Here, we use a 5^{th} order Taylor expansion of the sine term about the previous value of ψ_1. We choose the real root of the resulting polynomial that is closest to the previous value as the solution. While this procedure worked well for our data set (generally there was only one non-complex root), a more careful solution of (5) that is guaranteed to find all possible critical points as well as resolve the path-dependence issue represent works in progress.

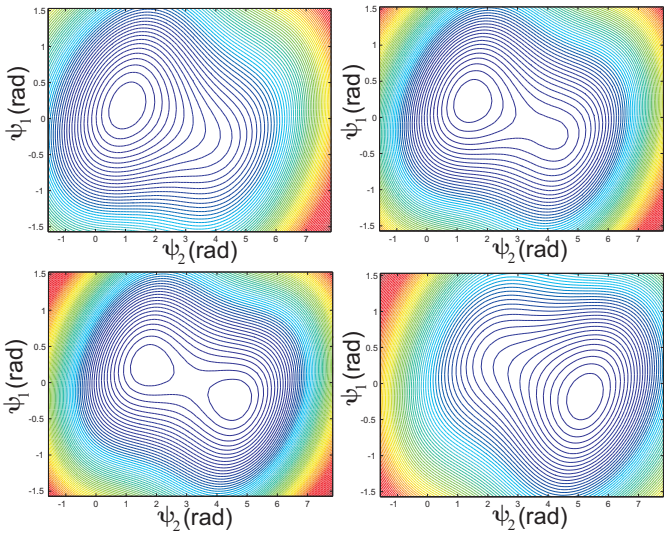

Fig. 5. Contour plots of the energy landscape as the angular difference between the tube bases is increased. (Top Left) 120° (Top Right) 160° (Bottom Left) 180° (Bottom Right) 240°. For small angular differences between the tubes, there is only one global minimum. As the angular difference approaches 180°, two appear. Beyond 180°, the new minimum becomes the global minimum, and eventually the only minimum. These plots are for the 'partial overlap' experiment in Section VI and are made using nominal parameter values.

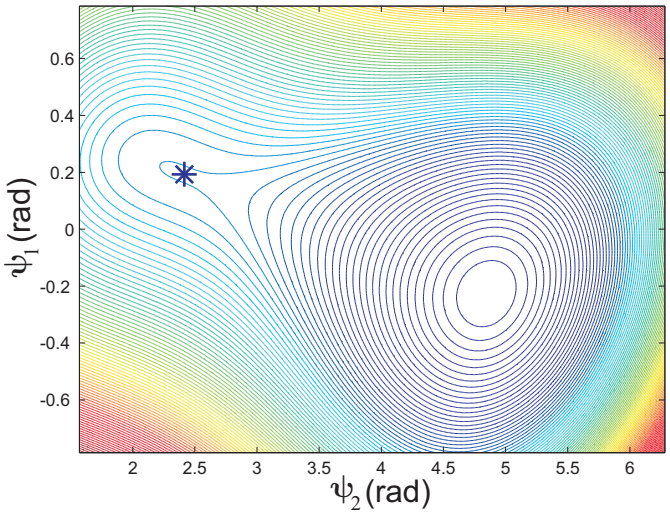

Fig. 6. Contour plot of the energy function at the bifurcation point. The * denotes the position of the system (from (9) and (10)) just before it bifurcates to a new minimum.

In the context of the current work, we found it sufficient to frequently visually inspect the roots returned, and to evaluate (6) with the ψ_1 value obtained to ensure that the numerical values of the left and right hand sides are approximately equal. We note that in practice on a robotic system, a close approximation for the true value of ψ_1 about which to expand is readily available, because the robot will only move a small amount between computer servo cycles.

A. Bifurcation and "Snapping"

As the difference between actuator input rotations $(\alpha_2 - \alpha_1)$ approaches 180°, a bifurcation in the energy landscape in the torsion angles (ψ_1, ψ_2) introduces two spurious critical points: a saddle and local minimum (see Figure 5). As actuator input difference approaches 180° from below, the new minimum deepens, and the minimum in which the system rests rises, until at $(\alpha_2 - \alpha_1) = 180°$ the heights of the minima are equal. Just beyond an actuator difference of 180°, the spurious minimum actually becomes the global minimum, but the system remains in the original local minimum due to the "torsional windup" history effect. As the input angle difference continues to increase, the system remains in the local minimum until it reaches another bifurcation, at which point the local minimum disappears, leaving only the global minimum above 180°. At this point the system "snaps" to the global minimum, releasing built-up torsional energy.

At a bifurcation point, a local minimum and saddle merge. This effect happens when the Hessian is singular (concavity changes) while simultaneously the gradient is zero (critical point). This is illustrated in Figure 6. The Hessian is singular when

$$\det\left(\frac{\partial^2 U}{\partial \psi^2}\right) = c_1 c_2 + (c_1 + c_2)\ell_2 c_3 \cos(\psi_1 - \psi_2) = 0. \quad (8)$$

Combining this with the zero gradient constraint (5), it is possible (for a fixed α_1) to solve for the ψ_1, ψ_2 and input α_2 at which the bifurcation occurs. These are given by,

$$\psi_1 = \frac{1}{c_1}\sqrt{(\ell_2 c_3)^2 - \left(\frac{c_1 c_2}{c_1 + c_2}\right)^2}, \quad (9)$$

$$\psi_2 = \psi_1 + \cos^{-1}\left(-\frac{c_1 c_2}{\ell_2 c_3 (c_1 + c_2)}\right), \quad (10)$$

$$\alpha_2 = \sqrt{(\ell_2 \beta)^2 + \cos^{-1}\left(\frac{1}{\ell_2 \beta}\right)}, \quad (11)$$

where the bifurcation parameter $\beta = -c_3/c_2 - c_3/c_1$. In Section VI-C we experimentally determine input angles that cause bifurcation, and use closed-form expression (11) to facilitate bifurcation parameter fitting.

VI. Experiments and Parameter Fitting

Two types of experiments were undertaken to evaluate the ability of the model discussed above to capture bifurcation behaviour and cannula shape. A second goal of these experiments was to calibrate the active cannula, estimating model parameters.

A. Experimental Setup

Our experimental prototype consists of a 1.60 mm diameter wire and a tube with 2.39 mm outside diameter (OD) and 2.01 mm inside diameter (ID). The wire has a 218.5 mm straight transmission and an 85 mm long circular curved section created via plastic deformation with a curvature of 0.0138/mm. The tube has a a 93.5 mm straight transmission and a 92.3 mm curved section created via plastic deformation with a curvature of 0.0099/mm. Both tube and wire have acrylic discs affixed to their base as shown in Figure 7. The discs are etched with radial lines every 10° to enable manual axial rotation to desired angles. The linear translations of the discs can be set using a scale etched onto the acrylic support structure. Locking mechanisms consisting of spring-loaded pins are available to fix wheel positions in both degrees of freedom.

Fiducial markers (bands of black tape) are placed along the cannula for stereo triangulation as shown in Figure 8. The positions of these fiducials are sensed using a stereo vision system composed of two calibrated Sony XCD-X710 firewire cameras. One source of error in this data collection procedure is the accuracy of manual point selection in images, which is estimated at 2 pixels or 0.6 mm. Another is fiducial size (they are not perfect points), causing small differences in intended selection locations. We estimate fiducial dimensions to introduce error of no more than the diameter of the wire itself (1.6 mm). Thus the overall vision system measurement error is estimated to be approximately 2.2 mm.

B. Parameter Estimates from Physical Quantities

Writing model parameters in terms of basic material properties and measured dimensions is the first step in determining reasonable physical expectations of parameter values. This can

be accomplished by combining (7) with the formula for cross-sectional inertia of a circular section ($I = \frac{\pi}{64}(OD^4 - ID^4)$), and the relationships between shear and bending quantities ($J = 2I$ and $E = 2G(1+\nu)$ where ν is Poisson's ratio), to produce

$$b_1 = \frac{E_2 I_2 L_1 k_1 k_2 (1+\nu_1)}{E_1 I_1 + E_2 I_2}, \quad b_2 = \frac{E_1 I_1 L_2 (1+\nu_2)}{E_2 I_2 L_1 (1+\nu_1)}. \quad (12)$$

Expected parameter ranges for b_1 and b_2 can be deduced from the uncertainty in each quantity upon which they depend. Nitinol dimensions are specified by the manufacturer (Nitinol Devices and Components, Inc.) to ± 0.0010 inch, while the elastic modulus E is reported as 41–75MPa. Poisson's ratio is not quoted, but is often taken to be approximately 0.35 for Nitinol. It has also been noted that plastic deformation can increase Poisson's ratio for Nitinol to 0.5 or more [18], so we will assume a range of 0.30–0.55. Measurement errors in straight transmission lengths are estimated to be 1 mm, and measurement accuracy of curvature was estimated at 10% (see [17]). Applying error propagation, the variance in parameters can be determined by[1]

$$\Omega_b = J_{b\varsigma}\, \Omega_\varsigma\, J_{b\varsigma}^T \quad (13)$$

where Ω_ς is a diagonal matrix of variances in each quantity upon which b_1 and b_2 depend (denoted by ς), and $J_{b\varsigma}$ is the Jacobian between parameters and quantities containing error $\left(J_{b\varsigma} = \frac{\partial b}{\partial \varsigma}\right)$. The square roots of the diagonal entries of Ω_b yield the variance in parameter values. These yield a b_1 range of 3.36–7.06 and a b_2 range of 3.14–8.45. A similar calculation for the bifurcation parameter ($\beta = -b_1(b_2+1)$) yields a range for β of (-41.45)–(-29.41). These ranges provide a basis for comparison with fitted parameter values produced by the calibration procedures described below.

[1]For the sake of estimating parameter variances, we assume that physical parameter ranges are equally-scaled variances.

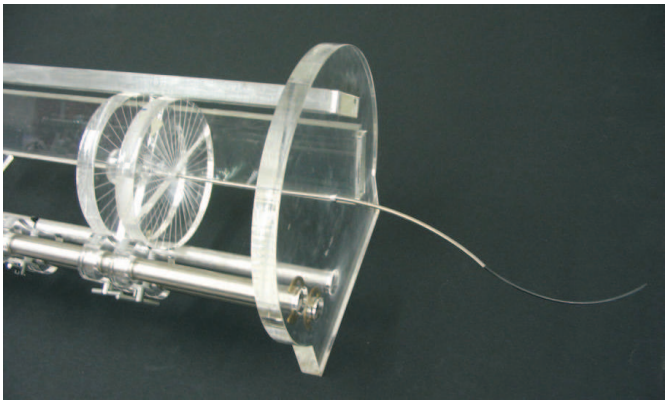

Fig. 7. Experimental apparatus. Both tube and wire have input circular handles etched to encode rotation and the support structure features a linear ruler etched to encode translation. Spring pin locking mechanisms hold wheels at desired linear and angular positions.

ℓ_2 (mm)	82.3	72.3	62.3	52.3	42.3	32.3	27.3
α_2 (deg)	295	283	265	240	225	205	200

TABLE I

SAMPLE EXPERIMENTAL BIFURCATION ANGLES FOR VARIOUS LENGTHS OF CURVED TUBE/WIRE OVERLAP

C. Bifurcation Point Experiment

To experimentally determine the bifurcation parameter β for the cannula, the tube was fixed in place and the wire was rotated until the bifurcation angle was reached. This was done for twelve linear translational positions in 5 mm increments for ℓ_2 from 82.3 to 27.3 mm. A sampling of this data is shown in Table I. Note that the input angle at which bifurcation occurs is always more than 180°, and often significantly more. This illustrates the torsional windup that occurs in active cannulas. The β parameter was fit to this data using Matlab's `nlinfit`, which computes a nonlinear regression using least squares. Using this procedure, we estimated β at -44.91, with a 95% confidence interval of ± 2.02, which is which is near (though slightly above) the ranges described in Section VI-B. In Section VI-D we explain how unmodeled effects should be expected to increase the magnatude of the experimental β in this type of experiment, but we first determine β again in Section VI-D through a different procedure that uses data more uniformly distributed over cannula workspace.

An important feature of active cannula bifurcation behavior is that it ceases to occur for some values of β. For a given cannula with fixed curvatures, this corresponds to a minimum length of curved tube overlap. Below this length, the energy landscape always has a single global minimum and thus it is not possible to simultaneously satisfy (5) and (8). The predicted ℓ_2 from (11) is 22.3 mm (the value at which $\cos^{-1}(\frac{1}{\ell_2 \beta})$ becomes undefined). Minima at slightly larger ℓ_2 values will be very near one another (and very near 180°), and friction will also mask very small bifurcation motions. These effects cause a first discernible experimental cannula bifurcation at ℓ_2 = 27.3 mm, slightly higher than the theoretical value. Given arclengths, it is also possible to choose Cannula curvatures so that bifurcation is prevented even for complete overlap. For fixed curvatures, we will further explore ℓ_2 prediction in the next section.

D. Shape Experiment

Using the stereo camera system described above and with the base of the tube fixed, cannula shape information was captured for multiple angles at two distinct linear positions of the base of the wire. One, called the "full overlap" position caused $\ell_1 = 10$ mm (tube curved, wire straight), $\ell_2 = 82.3$ mm (both curved), and $\ell_3 = 2.7$ mm (tube ended, only curved wire present). The other, called the "partial overlap" position caused $\ell_1 = 48.0$ mm, $\ell_2 = 44.3$ mm, and $\ell_3 = 40.7$ mm, with the same tube and wire combinations in each link. For the full overlap case, 15 input angles were applied at 20° increments from 0° to 280°. For the partial overlap case, 11 input angles were applied at 20° increments from 0° to 200°.

Using data collected from these experiments, we fit b_1 and b_2. The transformation between the stereo camera coordinate frame and a frame fixed at the base of the cannula was first estimated by applying Arun's method for point cloud registration [1]. Images of a 15 mm checkerboard pattern (with corners at known physical locations with respect to the cannula base frame) were captured. Sixteen corners on the checkerboard were triangulated with the stereo vision system. Since the points were coplanar, this registration was only expected to provide a rough estimate of the frame transformation. Thus six "nuisance parameters" (a 3-vector for position and a 3-vector for orientation with magnitude of rotation encoded as length) describing the cannula base frame were included in the calibration procedure, and initialized with the results from the point cloud registration.

Parameter fitting was accomplished using Matlab's `fmincon`, with angular nuisance parameter bounds set to ± 0.349,[2] from initial estimates. The objective function was the sum of Euclidean distances from experimental to theoretical tip positions (Eq. 4), outer tube endpoints (Eq. 4 up to link $m-1$), and positions of fiducial band nearest the cannula base (a fixed distance along the straight cannula transmission between T_0 and T_1). The optimization rapidly converged to $b_1 = 7.92$ and $b_2 = 4.11$ from a wide range of initial b_1 and b_2 values. Nuisance parameters showed only small changes during optimization, with cannula base frame orientation moving 4.4° while position of the base tape fiducial translated 1.1 mm. These small changes in nuisance parameters are reasonable given the coplanar data used to compute our initial frame transformation estimate. Average tip error was reduced from 10.1 mm (22.10 mm max) with no fitting to 3.0 mm (8.76 mm max) with fitting. Given estimated measurement error of 1 mm in individual tube straight and curved lengths, and the estimated 2.2 mm error in vision system data, a final average tip error of 3 mm appears reasonable.

Furthermore, the fitted b_2 was within the range determined in section VI-B, while b_1 was near it. The energy bifurcation parameter they imply ($\beta = -40.49$) is also now within its estimated parameter range. Small differences in β compared to the bifurcation experiment (which produced $\beta = -44.91$) are the results one would expect from unmodeled torsional deformation (in the curved regions) and unmodeled friction. Both would serve to increase the magnatude of the bifurcation experiment estimate of β. In that experiment all data was from regions in joint space where the highest possible cannula internal forces occur. This contrasts the shape experiment, which used data more uniformly distributed over the joint space. If effects of friction and unmodeled torsion cause a 5.4% reduction in each experimental bifurcation angle (see Table I), this would account for the difference in β. Further, $\beta = -40.49$ generates the prediction that bifurcation will cease at $\ell_2 = 24.7$ mm, only 2.6 mm less than the experimental value ($\ell_2 = 27.3$ mm found in VI-C), and somewhat closer than the $\ell_2 = 22.3$ mm determined in the bifurcation experiment.

[2]This is equivalent of $\pm 20°$ converted to radians. However, since magnitude is also encoded in these variables, this bound cannot be strictly thought of as an angle.

Fig. 8. Experimental photo from one of the stereo cameras showing the cannula with fiducial markers.

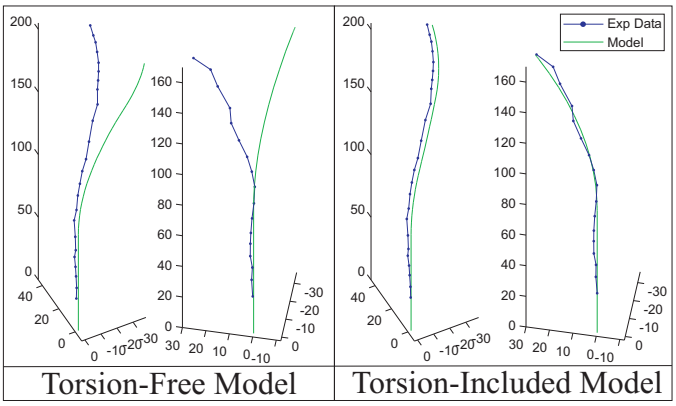

Fig. 9. Shown above are the final angle of the partial and full overlap positions (200° and 280° respectively), the data points with the greatest overall tip error for each case above. Overlaid model predictions clearly show that torsion is a vital part of an accurate active cannula kinematic model.

E. The Importance of Torsion

As we have described in this paper, including torsion in active cannula models leads to transcendental equations. Because of this (as outlined in Section II), models have been proposed in the literature that have assumed infinite torsional rigidity and treat active cannula kinematics as a pure beam bending problem. While this is analytically attractive, our experimental results indicate that assuming infinite torsional rigidity precludes accurate prediction of active cannula shape. Without torsion, there is only one model parameter present in the kinematic model (2), namely the ratio of tube flexural rigidities ($B = \frac{E_1 I_1}{E_2 I_2}$). The range for B estimated via the tolerances described in Section VI-B is 0.630–4.33.

Applying the same fitting procedures described in Section VI-D to the torsion free case, we first determined a tip error of 24.78 mm (54.32 mm maximum). We then fit model and frame nuisance parameters and found convergence over a wide range of initial values to B = 3.98, nuisance angle = 36.93°, and nuisance distance = 1.11 mm. Average tip error was reduced to 13.60 mm (31.48 mm maximum). Thus, tip errors remain large for the torsionless model even with calibration. Further,

the angular nuisance parameters changed significantly during the optimization, resulting in highly inaccurate predictions of overall cannula shape throughout the workspace.

To explore the possibility that nuisance parameters were not well suited for torsionless calibration, we also applied calibration procedures to the torsionless model while holding the nuisance parameters fixed values known to give approximately correct frame transformations. Fixing nuisance parameters at initial estimates from Arun's method, we optimized B alone and determined a value of 3.59. This resulted in average tip error of 23.50 mm (53.94 mm max). The other approximately correct set of nuisance parameters available are the calibrated values found for the torsion-included model in Section VI-D. Holding nuisance parameters fixed at these values, we determined B = 3.98. This resulted in an average tip error of 22.20 mm (52.39 mm).

All of the above efforts to calibrate the torsionless active cannula model result in large tip errors. This indicates that active cannula models that do not include torsion are structurally insufficient for making accurate predictions of our experimental active cannula shape. They also do not predict bifurcation behavior, since infinite torsional rigidity implies that tube angles are equal to base input angles at all points along the cannula. Results are illustrated visually in Figure 9 for a parameter value in the middle of the physically expected range, and using the initial frame estimate. If the cannula design were modified to use a different material with higher torsional rigidity for straight transmissions, the torsionless model may be more successful. However, doing so would be challenging from a prototype manufacturing standpoint. For our current all-Nitinol prototype, inability to account for torsional windup in the torsionless model makes it inaccurate except in a small neighborhood of $(\alpha_2 - \alpha_1) = 0$.

VII. Conclusion

Building upon the initial beam-mechanics-based models of tube interaction in one link of an active cannula [11], [17], we have described a general kinematic framework for multi-link cannulas that includes torsion in transmission. We also explored in detail the two-tube, three-link case, and experimentally calibrated model parameters using two different methods that agree well with one another and also produce results near parameter ranges derived from material property tolerances and physical geometry. Experimental results lead to the conclusion that when modeling active cannulas, torsion must be taken into account.

These results pose future research areas for active cannula designers, including solving standard robotics problems for active cannulas (e.g. compute differential or inverse kinematics) in an analytically more complex setting without the aid of closed form kinematics. Alternatively, one could approach the problem from a design perspective and try to construct active cannulas that more closely approximate torsionless kinematics, perhaps using innovative materials (e.g. the windings in flexible drive shafts).

The results presented in this paper are a steps toward realizing the potential of active cannulas, which we believe can give doctors the ability to reach previously inaccessible locations in the human body to treat disease much less invasively. The kinematics and calibration described here enable further advancement toward a complete theory of active cannulas, enhancing their utility in both medical and non-medical domains.

Acknowledgment

This work was supported in part by a National Science Foundation Graduate Fellowship and the Johns Hopkins University.

References

[1] K. S. Arun, T. S. Huang, and S. D. Blostein. Least-squares fitting of two 3-D point sets. *IEEE Transactions on Pattern Analysis and Machine Intellegence*, 9(5):698–700, 1987.

[2] G. S. Chirikjian. Kinematic synthesis of mechanisms and robotic manipulators with binary actuators. *Journal of Mechanical Design*, 117:573–580, 1995.

[3] P. Dario, M. C. Carrozza, M. Marcacci, S. D'Attanasio, B. Magnami, and G. M. O. Tonet. A novel mechatronic tool for computer-assisted arthroscopy. *IEEE Transactions on Information Technology in Biomedicine*, 4(1):15–29, 2000.

[4] W. Daum. A deflectable needle assembly, 2003. Patent 6,572,593.

[5] J. Furusho, T. Katsuragi, T. Kikuchi, T. Suzuki, H. Tanaka, Y. Chiba, and H. Horio. Curved multi-tube systems for fetal blood sampling and treatments of organs like brain and breast. *Journal of Computer Assisted Radiology and Surgery*, pages 223–226, 2006.

[6] M. W. Hannan and I. D. Walker. Kinematics and the implementation of an elephant's trunk manipulator and other continuum style robots. *Journal of Robotic Systems*, 20(2):45–63, 2003.

[7] B. A. Jones, W. McMahan, and I. D. Walker. Practical kinematics for real-time implimentation of continuum robots. *IEEE International Conference on Robotics and Automation*, pages 1840–1847, 2006.

[8] M. Loser. A new robotic system for visually controlled percutaneous interventions under X-ray or CT-fluoroscopy. Master's thesis, The Albert-Ludwig-University, Freiburg, Germany, September 2002.

[9] R. M. Murray, Z. Li, and S. S. Sastry. *A Mathematical Introduction to Robotic Manipulation*. CRC Press, Boca Raton, FL, 1994.

[10] S. Okazawa, R. Ebrahimi, J. Chuang, S. E. Salcudean, and R. Rohling. Hand-held steerable needle device. *IEEE/ASME Transactions on Mechatronics*, 10(3):285 – 296, 2005.

[11] P. Sears and P. E. Dupont. A steerable needle technology using curved concentric tubes. *IEEE/RSJ International Conference on Intelligent Robots and Systems (IROS)*, pages 2850–2856, October 9-15 2006. Beijing, China.

[12] P. Sears and P. E. Dupont. Inverse kinematics of concentric tube steerable needles. *IEEE International Conference on Robotics and Automation*, pages 1887–1892, 2007.

[13] N. Simaan, R. Taylor, and P. Flint. A dexterous system for laryngeal surgery. *IEEE International Conference on Robotics and Automation*, pages 351–357, 2004.

[14] R. J. Webster III. *Design and Mechanics of Continuum Robots for Surgery*. Mechanical engineering, Johns Hopkins University, Baltimore, MD, December 2007.

[15] R. J. Webster III, J. S. Kim, N. J. Cowan, G. S. Chirikjian, and A. M. Okamura. Nonholonomic modeling of needle steering. *International Journal of Robotics Research*, 25(5/6):509–526, May/June 2006.

[16] R. J. Webster III, J. Memisevic, and A. M. Okamura. Design considerations for robotic needle steering. *IEEE International Conference on Robotics and Automation*, pages 3599–3605, 2005.

[17] R. J. Webster III, A. M. Okamura, and N. J. Cowan. Toward active cannulas: Miniature snake-like surgical robots. *IEEE/RSJ International Conference on Intelligent Robots and Systems*, pages 2857–2863, October 9-15 2006. Beijing, China (Finalist for Best Paper Award).

[18] P. M. White. Stress induced interposed connector, 2001. Patent 6,257,593.